This document is published in:

Materials Science & Engineering. A, Vol. 606 (june 2014), pp. 276-289

DOI: http://dx.doi.org/10.1016/j.msea.2014.03.078

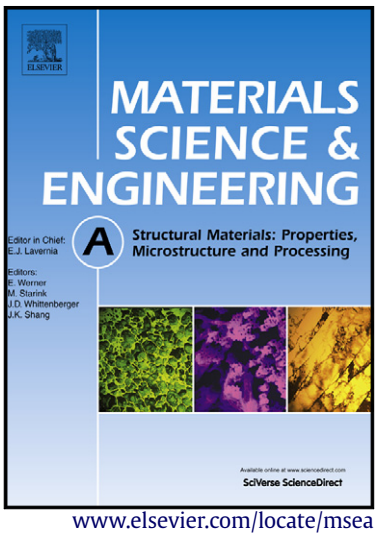

www.elsevier.com/locate/msea

Analysis of crystallographic slip and grain boundary sliding in a Ti-45Al-2 Nb-2Mn (at. %)-0.8v.%TiB_2 alloy by high temperature *in situ* mechanical testing

R. Muñoz-Moreno, E.M. Ruiz-Navas, C.J. Boehlert, J. Llorca, J.M. Torralba, M.T. Pérez-Prado

PII: S0921-5093(14)00360-8
DOI: http://dx.doi.org/10.1016/j.msea.2014.03.078
Reference: MSA30927

To appear in: *Materials Science* & *Engineering A*

Received date: 19 January 2014
Revised date: 20 March 2014
Accepted date: 21 March 2014

Cite this article as: R. Muñoz-Moreno, E.M. Ruiz-Navas, C.J. Boehlert, J. Llorca, J.M. Torralba, M.T. Pérez-Prado, Analysis of crystallographic slip and grain boundary sliding in a Ti-45Al-2 Nb-2Mn (at.%)-0.8v.%TiB_2 alloy by high temperature *in situ* mechanical testing, *Materials Science* & *Engineering A*, http://dx.doi.org/10.1016/j.msea.2014.03.078

Analysis of crystallographic slip and grain boundary sliding in a Ti-45Al-2Nb-2Mn (at.%)-0.8v.%TiB_2 alloy by high temperature *in situ* mechanical testing

R. Muñoz-Moreno[1, 2], E. M. Ruiz-Navas[2],

C. J. Boehlert[1, 3], J. Llorca[1,4], J.M. Torralba[1,2], M. T. Pérez-Prado[1,*]

[1] IMDEA Materials Institute, C/Eric Kandel 2, 28906, Getafe, Madrid, Spain
[2] Department of Materials Science and Engineering, Universidad Carlos III de Madrid, Avda. Universidad 30, 28911 Leganés, Spain.
[3] Department of Chemical Engineering and Materials Science, Michigan State University, 2527 Engineering building, East Lansing, MI 48824, USA.
[4] Department of Materials Science, Polytechnic University of Madrid, E. T. S. de Ingenieros de Caminos, 28040 Madrid, Spain
*Corresponding author. Phone: +34 915493422; Fax: +34 915503047; Email: teresa.perez.prado@imdea.org

Abstract

This work aims to contribute to a further understanding of the fundamentals of crystallographic slip and grain boundary sliding in the γ-TiAl Ti-45Al-2Nb-2Mn (at.%)-0.8v.%TiB_2 intermetallic alloy, by means of *in situ* high-temperature tensile testing combined with electron backscatter diffraction (EBSD). Several microstructures, containing different fractions and sizes of lamellar colonies and equiaxed γ-grains, were fabricated by either centrifugal casting or powder metallurgy, followed by heat treatment at 1300 ºC and furnace cooling. *In situ* tensile and tensile-creep experiments were performed in a scanning electron microscope (SEM) at temperatures ranging from 580 ºC to 700 ºC. EBSD was carried out in selected regions before and after straining. Our results suggest that, during constant strain rate tests, true twin γ/γ interfaces are the weakest barriers to dislocations and, thus, that the relevant length scale might be influenced by the distance between non-true twin boundaries. Under creep conditions both grain/colony boundary sliding (G/CBS) and crystallographic slip are observed to contribute to deformation. The incidence of boundary sliding is particularly high in γ grains of duplex microstructures. The slip activity during creep deformation in different microstructures was evaluated by trace analysis. Special emphasis was placed in distinguishing the compliance of different slip events with the Schmid law with respect to the applied stress.

Key words: *in situ* testing, EBSD, TiAl, crystallographic slip, grain boundary sliding, Schmid law.

1. Introduction

Gamma titanium aluminides are high-temperature structural intermetallics with better specific mechanical properties than superalloys [1, 2]. Therefore, they are being targeted by aerospace industries aiming to build lighter and stronger engine components such as, for example, low pressure turbine blades [3-5]. Extensive research efforts during the past two decades [6-10] have resulted in the development of γ-TiAl alloys with a balanced combination of properties (room temperature elongation-to-failure, fracture toughness, high-temperature strength, creep resistance and oxidation behavior), and some of these alloys have already found commercial uses [11, 12]. Future research should be aimed at enhancing the high-temperature capabilities of these materials. To this end, an improved knowledge of the deformation mechanisms active under service conditions would help to optimize the microstructural design of γ-TiAl alloys for a wider range of engineering applications.

Engineering γ-TiAl based alloys are dual-phase materials formed by α_2 (Ti_3Al, hexagonal close packed (hcp), DO_{19}) and γ (TiAl, face centered tetragonal (fct), $L1_0$) intermetallic compounds [6]. The morphology of these two components is highly dependent on the processing conditions and has a critical influence on the mechanical behavior. In general, microstructures containing two-phase lamellar colonies, named fully lamellar (FL), are endowed with high strength as well as excellent creep resistance. Duplex microstructures, in which different volume fractions of equiaxed γ grains are embedded in a matrix of lamellar colonies are however, softer and usually possess higher room temperature elongation-to-failure. Plastic strain accommodation of γ-TiAl based alloys at a wide range of temperatures and quasi-static strain rates has been reported to be mainly carried out by the softer γ phase through dislocation motion and mechanical twinning [6]. Activation of the latter has been found to be important to attain a

sufficient number of deformation modes for strain compatibility [13]. In addition, diffusion-based mechanisms such as grain/colony boundary sliding (CBS) have been observed to contribute to deformation at high temperatures and low strain rates [14, 15]. Compared to dislocation motion and mechanical twinning, little attention has been paid to CBS in γ-TiAl alloys. Thus, the influence of microstructure on the incidence of this mechanism as well as the prevailing accommodation mechanisms, are not understood.

Dislocation slip in fct γ-TiAl occurs preferentially on {111} planes along 110 directions. Since the latter are crystallographically not equivalent, two types of dislocations can be distinguished: ordinary dislocations (OD), with Burgers vector $\bar{b}_o = 1/2110]$ and superdislocations (SD), for which $\bar{b}_s = 101]$ and $\bar{b}_s = 1/211\bar{2}]$. Table 1 summarizes the twelve slip systems available as well as the dislocation type corresponding to each one [16]. Slip of OD has been found to prevail over SD activity in a wide range of two phase γ-TiAl alloys microstructures [17, 18]. The activation of SDs is a complex function of temperature and alloy composition [19-23]. An increase in the aluminum content as well as high levels of interstitial impurities in the γ- phase [24, 25] appear to promote SD activity. However, the intricate nature of the microstructures of γ-TiAl alloys, governed by a large number of parameters (composition, colony and grain size, lamella size, volume fraction of the two phases, misorientation and character of the interfaces), makes isolating the correlation of one microstructural feature to the dislocation activity difficult. A better knowledge of the fundamentals of crystallographic slip in these materials could be critical for enhancing alloy development.

Characterization of the dislocation activity in γ-TiAl intermetallics has been mostly carried out by transmission electron microscopy (TEM). While this technique allows resolving individual dislocations, it has inherent limitations [26], including the difficulty in sampling large volumes, the likelihood of removing dislocations during sample preparation and the damage of the thin area by beam irradiation, which might bias the analysis. *In situ* scanning electron microscopy (SEM) based mechanical testing is emerging as a complementary method to analyze slip activity in metallic materials [27-31]. This technique allows for the observation of the formation of slip traces at different strain levels in a relatively wide area of the surface

microstructure in real time and, with the aid of electron back-scattered diffraction (EBSD) [32], it facilitates the assignment of each slip trace to a specific slip system [31, 33-35], and, thus, the analysis of slip activity. This technique, which has not been utilized to date to investigate γ-TiAl alloys, would clearly be very helpful to understand the links between the microstructure and the activation of different deformation mechanisms in this intermetallic.

The aim of this work is to investigate crystallographic slip as well as colony and grain boundary sliding at high temperatures in a γ-TiAl alloy with different lamellar and duplex microstructures which were generated by centrifugal casting (CC) and powder metallurgy (PM). With this purpose, *in situ* testing in an SEM, aided by EBSD, was performed at temperatures ranging from 580 °C to 700 °C both at a constant strain rate of 10^{-3} s^{-1} and at a constant stress of 65%σ_{max}. Crystallographic slip and boundary sliding activation is linked to microstructural features such as the lamellae boundary misorientation and the presence of equiaxed γ grains. Slip activity during creep deformation is evaluated in different microstructures by slip trace analysis. Mechanical twinning, which is also an important deformation mechanism in this alloy, will not be treated in the present paper.

2. Experimental procedure

The γ-TiAl intermetallic alloy studied in this work had a nominal composition of Ti-45Al-2Nb-2Mn(at.%)-0.8vol.%TiB_2 (Ti4522XD) and it was processed by centrifugal casting (CC) and powder metallurgy (PM). The CC material, provided by GfE (Gesellschaft für Elektrometallurgie mbH, Nüremeberg, Germany), was centrifugally cast and subsequently hot isostatically pressed at 1185 ºC and 170 MPa during four hours in order to remove any remnant porosity at ACCESS e. V. TechCenter (Aachen, Germany) [36]. The CC bulk alloy composition (as measured by fluorescence) was (in at. %): 50.6 % Ti; 44.1 % Al; 2.0 % Nb; 2.2 % Mn; 0.04%

Si; 0.02% C; 0.86% O; 0.05% Fe; 0.04% H; 0.01% N; 0.86% B. The PM material was processed from prealloyed powders by hot isostatic pressing (HIP). The powders were obtained by electrode induction gas atomization (EIGA) [37] at the Helmholtz-Zentrum Geesthacht für Material und Küstenforschung GmbH (Geesthacht, Germany) and they were consolidated by HIP at 1200 ºC and 200 MPa during four hours under an Ar atmosphere at the Forschungzentrum Jülich (Jülich, Germany). Differential thermal analysis (DTA) was performed on a Setsys Evolution Setaram system (France) in order to determine the phase transformation temperatures for this specific alloy. From this data, it was confirmed that HIPing was always performed along $\alpha+\gamma$ phase diagram region.

Several tensile specimens were electrodischarge-machined from the CC and PM materials with a geometry provided in previous works [14, 15]. In order to evaluate the influence of the microstructure on the dominant deformation mechanisms, different microstructures were generated by heat treating selected CC and PM tensile specimens for two hours within the α-phase field (1300 ºC) followed by furnace cooling. The materials obtained after these treatments were called CCFC and PMFC, respectively. In order to minimize oxidation during the heat treatments, the tensile samples were wrapped in Ta foil and encapsulated in purged quartz tubes filled with Ar. The heating rate was 10 ºC/min.

The microstructure of the as-centrifugally cast (CC), CCFC and PMFC samples was examined by SEM and TEM. SEM analysis was carried out using a field emission gun SEM (FEG-SEM) Mira-Tescan (Brno, Czech Republic). Samples for SEM examination were polished using silicon carbide paper as well as diamond paste and a 0.04 μm colloidal silica slurry. TEM analysis was performed using both a FEI Instruments (Oregon, USA) Tecnai T20 TEM at 200 kV and a JEOL JEM 2100 (Tokio, Japan) TEM at 200kV. The TEM foils were prepared by

grinding the samples to a thickness of approximately 200 μm, then punching 3 mm diameter disks, and finally thinning them using a Struers (Ballerup, Denmark) twinjet Tenupol-5 electropolisher until perforation. The electropolishing solution, which consisted of 5% perchloric acid, 35% butanol, and 60% methanol, was held at a constant temperature of -30°C. The voltage utilized was 40 volts. The average colony size, obtained from SEM measurements of approximately 90 colonies, was determined using the ASTM grain size standard [38]. The apparent average lamellar thickness of both phases, $\lambda_{\alpha 2}$ and λ_{γ}, was measured for the CC and CCFC samples. The CC measurements included 50 γ lamellae and 30 α_2 lamellae. CCFC measurements included 30 γ lamellae and 29 α_2 lamellae. The lamellar spacing was measured using bright field TEM images in the "edge-on" condition, which was confirmed by tilting the TEM foil to the (0001) α_2 selected area diffraction pattern (SADP) which overlapped the (111) γ SADP. The α_2 lamellae thickness was identified using dark field imaging by isolating the (0001) α_2 spot. The γ lamellae thickness was then measured in the corresponding bright field images.

In situ tensile experiments were conducted on the CC and CCFC samples at a constant strain rate of $10^{-3}s^{-1}$ at 580 ± 30 °C and at 700 ± 30 °C. *In situ* tensile-creep tests were performed on the CCFC and the PMFC specimens at 700 ± 30 °C and constant stresses of either 325 MPa (CCFC) or 300 MPa (PMFC) (σ_{creep}=65%σ_{max}). All the tests were performed using a screw-driven tensile stage placed inside the SEM. A schematic view of the tensile testing machine inside the SEM chamber is shown in Figure 1a. The load was measured using a 4,448 N load cell. For the tensile-creep tests the load was applied at 250 N/min until reaching 90% of the desired creep stress (σ_{creep}) and at 25 N/min until reaching σ_{creep}. The temperature was controlled using a

constant-voltage power supply to a 6 mm diameter tungsten-based heater located just below the gage section of the sample. An open-bath, closed-loop chiller was used to circulate distilled water at room temperature through copper tubes to prevent the tensile stage from overheating. The sample's temperature was obtained during the test utilizing a fine-gage K-type thermocouple which was spot-welded to the sample's gage section. After the sample's gage-section temperature reached the desired test temperature, the sample was held at this temperature for at least 30 minutes prior to applying the load in order to thermally stabilize the system. The pressure in the SEM chamber never exceeded $4x10^{-6}$ torr in order to avoid oxidation. Back-scattered electron (BSE) SEM images were taken before and after the experiments and secondary electron (SE) SEM images were taken periodically during the tests. The strain values were estimated from the test machine's displacement measurements taking into account the heated gage length of the samples. Further details of this apparatus and testing technique can be found elsewhere [34, 35].

The microtexture was analyzed in selected areas of the CC, CCFC and PMFC specimens, before and after testing, by EBSD analysis in a FEG-SEM Mira-Tescan SEM (Brno, Czech Republic), equipped with an EDAX-TSL (Mahwah, NJ, USA) EBSD system. Sample preparation for EBSD analysis involved grinding using increasingly finer SiC paper, down to a grit size of 4000, followed by 4 h of polishing with a mixture of 0.04 μm colloidal silica and H_20_2. It is well known that for γ-TiAl alloys with 45-48% of Al, the α_2 and γ phase volume fractions lie between 5-20% and 80-95%, respectively [2]. In addition, as the γ phase is the one that carries most of the strain, only this phase was indexed. A challenge associated with EBSD examination of γ-TiAl alloys is the large difference in size between the width of individual

lamellae and the diameter of lamellar colonies (approximately 3 orders of magnitude). Thus, resolving individual lamellae required acquiring maps at high magnification, in which a limited number of colonies were included. In order to address this issue, orientation maps were obtained at several areas of the specimens´ gage length. Misorientation distribution histograms were analyzed for the *in situ* SEM studied areas before and after straining with the aim of analyzing the evolution of the nature of the boundaries during testing.

The activation of different slip systems was estimated from the analysis of the SEM micrographs acquired *in situ* during straining and the EBSD orientation maps of the same areas. This analysis was performed following a previously detailed methodology [33-35] consisting of the following steps. First, identification of a individual slip plane trace on the SEM micrographs in a given grain (Fig. 1b-(1,2)); second, calculation of the 12 plane traces corresponding to all slip systems by the cross product of the slip plane and the surface normal of the corresponding grain (Fig. 1b-(3)); third, selection of the slip systems whose traces match the one observed experimentally. Due to the geometry of the fct lattice each observed trace is shared by three slip systems (one OD and two SD, in red in Fig. 1b(4)). Thus, determination of the actual active slip system is not trivial. In this research work a methodology to classify the active slip systems is proposed and the compliance of these systems with the Schmid law is evaluated.

3. Results

Figure 2 illustrates the different microstructures of the studied γ-TiAl alloy. The CC and CCFC materials exhibited lamellar microstructures (Figs. 2 a, b), while the PMFC material exhibited a duplex microstructure combining lamellar colonies with some equiaxed grains (Fig. 2c). The average colony sizes in the CC and CCFC materials were 126±52 μm and 181±83 μm, respectively. The PMFC microstructure was formed by lamellar colonies that were 98±34 μm in

diameter and equiaxed gamma grains with an average size of 4±1 μm. The average lamellae thicknesses for the γ (λ_γ) and α_2 ($\lambda_{\alpha 2}$) phases in the CC alloy, are 465±270 nm and 290±290 nm, respectively. A significant lamellae refinement was found in the CCFC sample, where λ_γ was 210±140 nm, and $\lambda_{\alpha 2}$ was 160±160 nm. In all cases, the distributions are very wide (CC: λ_γ [51, 1000]nm, $\lambda_{\alpha 2}$ [31, 1260]nm; CCFC: λ_γ [35, 471]nm, $\lambda_{\alpha 2}$ [13, 578]nm), with standard deviations close to the average values, as has been previously reported for fully-lamellar TiAl alloys [39].

3.1 High temperature constant strain rate behavior of lamellar microstructures

The mechanical response of the CC and the CCFC alloys tested *in situ* at 580 °C and 700 °C and at a strain rate of 10^{-3} s^{-1} and, in particular, the values of the maximum flow stresses and the elongations to failure obtained, are summarized in Table 2. Flow stresses ranged from 450 MPa to 550 MPa and the elongation to failure varied between 1.3% and 1.9%.

Figure 3 depicts the EBSD inverse pole figure maps in the normal direction (ND) corresponding to selected areas of the CC sample before and after testing at a strain rate of 10^{-3} s^{-1} at 580 °C (Figs. 3a, b) and 700 °C (Figs. 3d, e). The SEM micrographs corresponding to the same areas in the post-test state (ε_{max}=1.3% at 580 ºC and ε_{max}=1.6 % at 700 ºC) are also added as they provide a complementary visualization of the changes in the specimens' surfaces (Figs. 3c, f). Finally, Figs. 3g and 3h show the misorientation distribution histograms corresponding to the same areas before and after testing at both temperatures. Comparison of Figs. 3a and 3b reveals that changes in the orientation of some grains took place during the 580 ºC deformation suggesting the occurrence of lattice rotations by crystallographic slip. Such grains have been highlighted using a rectangle in the map. Significant changes in the misorientation distribution histogram took place upon straining (Fig. 3g). The pre-test histogram is formed mainly by three

sharp peaks located at misorientation angles (θ) of 60 °, 70 °, and 90 °, which correspond to boundaries between the three main γ variants, namely, pseudotwins (60 º around $<111>_{\gamma}$), order variants (120 º around $<111>_{\gamma}$) and true twins (180 º around $<111>_{\gamma}$) [6, 40, 41]. This histogram reveals that in the area of the microstructure tested at 580 °C that was mapped by EBSD before testing (Fig. 3a), true twin interfaces were the most abundant, followed by order variants and pseudotwins (Fig. 3g). This is consistent with previous investigations, which revealed that true twin γ/γ boundaries occur more frequently due, at least partly, to their lower interfacial energy [6, 41]. After testing at 580 °C, the fraction of true twin boundaries decreased significantly. The fraction of pseudotwins and order variants decreased only slightly and the frequency of interfaces with all other misorientation angles increased (Fig. 3g). The dramatic decrease of the frequency of true twin boundaries upon deformation suggests a high incidence of crystallographic slip at true twin-related lamellae, leading to large lattice rotations on both sides of the boundary and, thus, to significant changes in the boundary misorientation angle. This is consistent with a lower resistance to slip transfer of true twin γ/γ interfaces. Although the barrier strength of the different γ/γ lamellae boundaries has not been measured previously, it has been speculated that true twin interfaces should be the softest because slip transfer could be accomplished by conjugate slip systems, which are in mirror symmetry [42].

In the area of the microstructure tested at 700 °C that was mapped by EBSD before and after testing (Figs. 3d-e), however, no major variations in the orientation of the grains were detected. After deformation (ε=1.6 %) the corresponding misorientation distribution histogram (Fig. 3h) reveals that, in this particular region, the fraction of true twin boundaries was relatively low and, moreover, similar to that of order variants. In agreement with the above observations, no significant changes took place in the boundary misorientation histogram. This data suggests

that slip does not take place homogeneously throughout the microstructure. Regardless the temperature, the incidence of crystallographic slip appears to be related to the fraction of true twin boundaries. SEM examination (Fig. 3f) revealed, additionally, the appearance of interlamellar ledges (white arrows) and incipient colony boundary relief (red arrows), that were identified *in situ* at strains of 1.1 % and 1.4 %, respectively. These SEM observations are consistent with a moderate enhancement of diffusion-based mechanisms at higher temperatures.

Figure 4 depicts the EBSD inverse pole figure maps in the ND corresponding to selected areas of the CCFC sample before and after testing at a strain rate of 10^{-3} s^{-1} at 580 °C (Figs. 4a, b) and 700°C (Figs. 4d, e). The SEM micrographs of the same areas in the post-test state (ε_{max}=1.8 % at 580 ºC and ε_{max}=1.9 % at 700 ºC) are also added as they provide a complementary visualization of changes in the deformed surface (Figs. 4c, f). Finally, Figs. 4g and 4h show the misorientation distribution histograms corresponding to the same areas before and after testing at both temperatures. Changes in the orientation of some grains (highlighted using rectangles) are clearly visible at both temperatures, suggesting the occurrence of crystallographic slip. The inverse pole figures showing the orientation on the tensile axis both before and after the tensile test at 580 ºC confirmed the occurrence of lattice rotations. In particular, 110 directions tended to align with the loading axis. The misorientation distribution histograms (Figs. 4g,h) revealed a predominance of true twin boundaries in the two areas examined. They also revealed a pronounced decrease in the frequency of such boundaries upon straining, giving rise to a higher background level. These observations are consistent with a prevalence of crystallographic slip at both temperatures and with enhanced slip transfer across true twin interfaces. The SEM micrographs (Figs. 4c,f) reveal the appearance of interlamellar ledges (white arrows) at 580 ºC and 700 ºC. Interlamellar ledges first appeared at strains of 1.7 % and 1.5 % in the 580 ºC and 700 ºC tensile-deformed samples, respectively. Moreover, at 700°C colony boundary relief (red arrow) is also detected at a strain of 1.9 % (Fig. 4f). This phenomenon is consistent with a higher contribution from diffusion-based mechanisms to the deformation as temperature increases.

3.2 High temperature constant stress behavior (creep) of lamellar and duplex microstructures

The total strain versus time creep curves corresponding to the CCFC and PMFC microstructures deformed at 700 ºC and 65%σ_{max} are plotted in Fig. 5a. No stress drops were observed since, due to the low strain rates involved (10^{-5} s^{-1} and 10^{-4} s^{-1}, respectively), it was possible to acquire SEM micrographs of the surface without interrupting the test. The lamellar

alloy (CCFC) was more creep resistant than the one with a duplex microstructure (PMFC). In particular, the secondary strain rate was higher and the creep life was shorter for the latter, as shown in the strain rate vs. time plot of Fig. 5b.

Fig. 6 illustrates a sequence of SEM micrographs showing the microstructural evolution for an area of the PMFC sample with increasing creep strain. After a deformation of 0.3 %, some relief was apparent both at the colony boundaries (colony size=98 μm) as well as at the boundaries of the equiaxed γ grains (grain size=4 μm). With increasing strain, cracking of the boundaries became more pronounced. These observations suggest the operation of boundary sliding during deformation. This is consistent with previous reports [14, 15]. Due to the relatively small size of the γ grains, a large surface area of boundaries was present. Boundary cracking initiated at strains as small as 1%. This phenomenon was also visible in the higher-magnification micrographs of Fig. 7 which reveal, additionally, crystallographic slip activity. The width of the slip traces and their number increased dramatically with deformation.

The microstructural evolution of the CCFC sample (colony size=181 μm) during creep under the same conditions is illustrated in Fig. 8. Although colony boundary relief leading to colony boundary cracking was also apparent during deformation, its incidence was significantly lower than in the PMFC sample. In particular, these two phenomena were only noticeable after strains of 1 % and 1.8 %, respectively. These strains, and especially the strain associated to the initiation of boundary cracking, were higher than those observed in the PMFC alloy. These differences are consistent with an enhanced resistance to boundary sliding in the CCFC sample associated to the larger colony size. Indications of crystallographic slip activity (Fig. 8e) were also evident in the lamellar microstructure of the CCFC sample.

4. Discussion

4.1. Critical length scales in lamellar γ-TiAl alloys

Monocrystalline γ-TiAl lamellar structures exhibit high plastic anisotropy as their yield stress and elongation-to-fracture strongly depend on the lamellar orientation with respect to the loading axis (ϕ). Many authors have worked on this issue through the study of polysynthetically twinned (PST) crystals [43-45]. When lamellae are perpendicular to the loading axis, shear is mostly transverse to different lamellae and dislocation pile ups occur at the lamellae interfaces (hard deformation mode). When ϕ is comprised between 30 ° and 60 ° shear occurs parallel to the lamellae interfaces and pile ups form preferentially at the domain boundaries (soft deformation mode). Due to the inherent complexity of polycrystalline γ-TiAl microstructures, it has proven difficult to relate the yield strength and a specific length scale (or a combination of them) using a Hall-Petch type law. A number of studies have attempted to carry out this task and a wealth of Hall-Petch constants (K_y) have been obtained [6]. Similarly, selection of the most critical length scale out of the many available (colony size, grain size, lamellar spacing, domain size) has proven challenging, as devising processing routes that allow controlling one microstructural feature while leaving all the others constant is difficult. Overall, it has become clear that different types of interfaces have to be taken into account to describe the strengthening of two phase γ-TiAl alloys, and the lamellar spacing (λ) seems to be the most influential of all [16].

Our results show that the frequency of true twin γ/γ lamella interfaces decreases dramatically with straining in both the CC and CCFC microstructures tested in tension at constant strain rate (10^{-3} s^{-1}) and at temperatures ranging from 580 °C to 700 °C, while those of

other γ/γ interfaces remain basically constant. This proves the relatively higher weakness of true twin γ/γ lamella interfaces with respect to that of pseudo-twin and order variant ones. Thus, at least in the alloy investigated, the critical length scale appears to be strongly influenced by the distance between non-true twin boundaries and, therefore, could be larger than λ.

4.2. Slip activity during creep deformation at 700℃ in lamellar and duplex microstructures

Estimating the activity of ordinary and superdislocations in γ-TiAl from the analysis of the surface slip plane traces observed by SEM is not trivial because each {111} slip plane is shared by one ordinary system and two superdislocation systems (Table 1) and, furthermore, the CRSS values corresponding to both types of dislocations for the alloy under study are not known. In order to investigate further dislocation activity, we have carried out the following trace analysis. First, we identified 100 slip traces in the creep-tested PMFC material (75 in equiaxed grains and 25 in the lamellae regions) and 29 slip traces (16 in equiaxed grains and 13 in the lamellae regions) in the creep-tested CCFC material. Detecting slip traces in the CCFC material proved more challenging due to the finer size of the lamellae as well as to the lower strains attained. Then, we divided the measured traces in three groups. The first one corresponds to traces with the highest Schmid factor of all ordinary and superdislocation systems. This group (Group 1) corresponds undoubtedly to dislocation events obeying the Schmid law with respect to the applied stress. A second group (Group 2) is formed by traces for which the opposite is true, i.e., with the smallest Schmid factors of all ordinary and superdislocation systems. These traces correspond to dislocation activity that does not obey the Schmid law with respect to the applied stress, i.e., such dislocations are activated as a consequence of the presence of local stresses. Finally, a third group (Group 3) is formed by traces for which there is uncertainty as to whether the Schmid law with respect to the applied stress is obeyed, as the Schmid factor of either the

ordinary or the superdislocation systems associated to such traces are smaller than the factors corresponding to other systems of similar type. The fraction of traces corresponding to each group for the CCFC and PMFC materials is summarized in Table 3. Similar proportions are observed for the two microstructures analyzed. In both materials, Group 1 is formed by 13 to 17 % of the traces, Group 2 is formed by 31 to 38 % and close to 50 % of the measured traces belong to Group 3.

4.2.1. Slip activity obeying the Schmid law with respect to the applied stress (Group 1)

In the following we propose a methodology to evaluate the activity of ordinary and superdislocations associated to Group 1 traces. A trace will be assigned to an ordinary dislocation when the resolved shear stress on the ordinary system (RSS_o) is higher than the CRSS of that system ($CRSS_o$) and, simultaneously, the resolved shear stress on the superdislocation system (RSS_s) with the highest Schmid factor out of the two systems sharing the same slip plane ($CRSS_s$) is lower than the CRSS of that system, i.e.:

$$RSS_o\ (MPa) = \sigma * SF_o > CRSS_o = R * CRSS_s \quad (1)$$

$$RSS_s\ (MPa) = \sigma * SF_s < CRSS_s \quad (2)$$

where SF_o is the Schmid factor of the ordinary system with respect to the applied stress (σ(PMFC)= 300 MPa; σ(CCFC)= 325 MPa;), SF_s is the Schmid factor of the superdislocation system, and R is the ratio between the critical resolved shear stress of ordinary and superdislocations ($R = CRSS_o / CRSS_s$). Conversely, a trace will be assigned to a superdislocation when inequalities (3) and (4) are true simultaneously:

$$RSS_o\ (MPa) = \sigma * SF_o < CRSS_o = R * CRSS_s \quad (3)$$

$$RSS_s\ (MPa) = \sigma * SF_s > CRSS_s \quad (4)$$

It is implicit in this analysis that each observed plane trace corresponds to a single slip system. The two above systems of inequalities are solved graphically for a given trace t_i in Fig. 9, which represents the variation of $CRSS_s$ with respect to R for that particular trace. The area shaded with squares corresponds to ($CRSS_s$, R) pairs for which the analyzed trace is assigned to ordinary dislocation slip, whereas the area filled with dots corresponds to ($CRSS_s$, R) pairs for which the trace is assigned to superdislocation activity. R_{ci} ($=SF_{oi}/SF_{si}$) is a critical R value that denotes the transition between ordinary and superdislocation slip, i.e., when $R< R_c$, t_i is assigned to ordinary dislocations and, conversely, when $R> R_c$, t_i is assigned to superdislocation slip.

The analysis described above was applied to Group 1 traces belonging to the gamma grains of the PMFC material, as the higher number of available traces allowed for better statistics (Table 4). The relative activity of ordinary and superdislocations is presented in Fig.10 for different R values. The figure reveals that superdislocation activity increases (and, in turn, ordinary slip activity decreases) linearly with respect to R with a slope equal to 0.14 % for both microstructures. Also, the activity of ordinary dislocations becomes negligible for R values higher than 1.5 and the activity of superdislocations is zero for R values lower than 1. The true R value corresponding to the Ti4522XD alloy under study is not known, as the critical resolved shear stresses of the different slip systems have never been measured. In fact, a wide dispersion of CRSS values has been reported for single crystalline γ-TiAl alloys, as reflected in Table 5. In general, it is believed that the activity of superdislocations increases with increasing Al content and that it is dependent on orientation, although these aspects are still controversial [13, 19]. Also, an anomalous temperature dependence of the CRSS of ordinary and superdislocations has been reported [19-23]. Both parameters exhibit a peak at temperatures between 700°C and 1000°C. Despite the little data available, Table 5 suggests that, in general, alloys with high Al

content (54-58 at.%) exhibit very high R values (1.5-1.9) at temperatures ranging from 25°C to 700°C. When the Al content decreases to 50 at.%, the R values measured are significantly lower (0.8). Although the R value for our Ti4522XD alloy is not known at any temperature, the low Al content would be consistent with values that are lower than those observed for highly alloyed systems, i.e., it is likely that R<1.5 (Table 5).

For a given R (for example, R_1 in Fig.9) there is an interval of $CRSS_s$ values $[CRSS_s' - CRSS_s'']_i$ for which trace t_i could be assigned to superdislocation slip. If $CRSS_s$ were unique for a given composition and microstructure, all $[CRSS_s' - CRSS_s'']_i$ should intersect exactly at that value. If several $CRSS_s$ values existed, which could be associated, for example, to different orientations, several clusters of $[CRSS_s' - CRSS_s'']_i$ intervals intersecting at different $CRSS_s$ values would exist. We have analyzed the intersections between the $[CRSS_s' - CRSS_s'']_i$ intervals corresponding to all the Group 1 traces detected in the grains of the PMFC sample for R values of 0.7, 1, and 1.5. In all three cases, almost all $[CRSS_s' - CRSS_s'']_i$ intervals intersected at one single $CRSS_s$ range, which was then taken as the best estimation of the $CRSS_s$ for the material under study. In particular, when R=0.7, $CRSS_s$=(126-177) MPa for 100% of the traces; when R=1, $CRSS_s$=(123-131) MPa for 91% of the traces; when R=1.5, $CRSS_s$=(97-98) MPa for 100% of the traces. The corresponding $CRSS_o$ values are, respectively, (88-124) MPa for R=0.7, (123-131) MPa for R=1, and (146-147) MPa for R=1.5.

4.2.2. Slip activity non-compliant with the Schmid law with respect to the applied stress (Group 2)

Table 3 reveals that, in the two microstructures analyzed, a large amount of the slip traces detected correspond to slip activity that does not comply with the Schmid law with respect to the applied stress. In particular, a minimum of 30 to 40% of the traces belong to Group 2.

Furthermore, Table 4 illustrates the fraction of Group 2 traces detected in the grains and the lamellae of the PMFC sample, evidencing that such events are frequent in both cases. A correlation between the spatial location of these traces with respect to lamellae or grain boundaries is not evident. The abundance of group 2 traces suggests that this type of slip activity should be taken into account in models aiming to provide a realistic description of the plasticity of these materials.

Non-Schmid behavior with respect to the applied stress in lamellar γ-TiAl structures has been reported earlier. Zupan and Hemker [20] observed it in a Ti-55.5 at.%Al intermetallic and Woodward and Rao [46] predicted its occurrence by ab-initio simulations as a consequence of the presence of small but significant edge atomic displacements near the core of ordinary dislocations, which could interact with stresses other than the resolved stresses on the glide plane. Additionally, non-Schmid behavior in lamellae could be caused by high local stress concentrations at the interfaces leading to preferential slip transfer to conjugate systems (which may not have the highest Schmid factor) in true twin-related lamellae [42].

The origin of the relatively high non-Schmid slip activity with respect to the applied stress observed in the present study in the equiaxed γ-grains of the PMFC duplex microstructure is, however, still not known. This behavior could be partly related to the accommodation of the high local stress concentrations at triple points resulting from the operation of grain boundary sliding [47]. The accommodation mechanisms proposed in the literature are either based on diffusion transport [48, 49] or on the movement of dislocations along grain boundaries or through the interior of the grains [50, 51]. The predominance of one or the other is still controversial. Some studies based on the analysis of marker lines and on the observation of the grain geometry in (sub)surface regions have concluded that diffusion accommodation prevails

[52, 53]. Other works, in which texture analysis was utilized as the main tool to investigate deformation mechanisms, report that dislocation slip acts primarily as an accommodation mechanism for grain boundary sliding in Mg and Al alloys [54, 55]. Analysis of slip traces during *in situ* testing could prove to be an excellent technique to contribute to this discussion since GBS accommodation by intragranular slip should give rise to non-Schmid slip behavior with respect to the applied stress, as dislocations would be activated in response to the high local stress concentrations at triple points. As revealed by Figs. 7 and 8, boundary sliding takes place profusely in the PMFC microstructure deformed under creep conditions and the incidence of this mechanism is particularly high along the boundaries of the equiaxed gamma grains. The present results, thus, are consistent with the operation of intragranular slip as an accommodation mechanism for GBS in duplex microstructures.

5. Conclusions

This work aims to analyze the high temperature deformation mechanisms of a Ti4522XD γ-TiAl alloy and, specifically, crystallographic slip and boundary sliding, by *in situ* mechanical testing in the SEM aided by EBSD. With that purpose, several duplex and lamellar microstructures were processed by centrifugal casting and by hot isostatic pressing of powders. A careful analysis of the evolution of the microtexture, the grain boundary distribution and the slip traces with straining under constant stress and constant strain rate conditions at high temperatures has led to the following conclusions:

1. True twin γ/γ interfaces appear to be weaker obstacles to dislocation movement than other types of lamellar boundaries. This points toward the fact that the critical length

scale of these materials might be influenced by the distance between non-true twin boundaries and, thus, be larger than the average lamella width.

2. Colony and grain boundary sliding are observed to be active deformation mechanisms under creep conditions. In particular, the incidence of sliding along the boundaries of equiaxed γ grains in duplex microstructures appears to be particularly high.
3. A methodology to estimate (a) the relative activity of ordinary and superdislocations and (b) the CRSS values of both slip modes in slip events obeying the Schmid law with respect to the applied stress is proposed.
4. A high amount (a minimum of 30-40%) of slip traces corresponding to slip events that do not comply with the Schmid law with respect to the applied stress and which, therefore, are activated by local stresses, was detected in both lamellar and duplex microstructures.
5. In duplex microstructures, the activity of slip systems that do not comply with the Schmid law with respect to the applied stress is equally frequent in lamellae and in equiaxed gamma grains. Its presence in the former is consistent with previous findings. In the latter, it may be associated to intragranular slip accommodation of grain boundary sliding.

Acknowledgements

Funding from the Spanish Ministry of Science and Innovation through projects (MAT2009-14547-C02-01 and MAT2009-14547-C02-02) is acknowledged. The Madrid Regional Government partially supported this project through the ESTRUMAT grant (P2009/MAT-1585). We also acknowledge financial support from the Spanish Ministry of Economy and Competitiveness through grant MAT2012-31889.

References

1. M. Yamaguchi, H. Inui, K. Ito, Acta Mater. 48 (2000) 307-322.
2. H. Clemens, S. Mayer, Adv. Eng. Mat. 15 (2013) 191-215.
3. F. Appel, U. Brossmann, U. Christoph, S. Eggert, S. Janschek, U. Lorentz, J. Müllauer, M. Oehring, J. D. H. Paul, Adv. Eng. Mat. 2 (2000) 699-720.
4. E. A. Loria, Intermetallics 8 (2000) 1339-1345.
5. K. Kothari, R. Radhakrishnan, N. M. Wereley, Prog. Aerosp. Sci. 55 (2012) 1-16.
6. F. Appel, J. D. H. Paul, M. Oehring, γ–Titanium Aluminides, Wiley-VCH, 2011.
7. T. A. Parthasaraty, P. R. Subramanian, M. G. Mendiratta, D. M. Dimiduk, Acta Mater. 48 (2000) 541-551.
8. H. Zhu, D. Seo, K. Maruyama, Mater. Trans. 45 (2004) 2618-2621.
9. J. Beddoes, L. Zhao, P. Au, D. Dudzinski, J. Triantafillou, editors, Structural Intermetallics, Warrendale PA TMS (1997) 109.
10. M. E. Kassner, M. T. Pérez-Prado, Fundamentals of creep in metals and alloys, Oxford, Elsevier, 2004.
11. B. P. Bewlay, Presentation at the European Symposium of superalloys and their applications, Wildbad Kreuth, Germany, 2010.
12. H. Clemens, W. Smarsly, Adv. Mater. Res. 278 (2011) 551-556.
13. H. Mecking, C. Hartig, U. F. Kocks, Acta Mater. 44 (1996) 1309-1321.
14. R. Muñoz-Moreno, C. J. Boehlert, M. T. Pérez-Prado, E. M. Ruiz-Navas, J. Llorca, Met. Mat. Trans. A 43 (2012) 1198-1208.
15. R. Muñoz-Moreno, M. T. Pérez-Prado, J. Llorca, E. M. Ruiz-Navas, C. J. Boehlert. Met. Mat. Trans. A 44 (2013) 1887-1896.
16. C. Zambaldi. Ph.D. Thesis, RWTH Aachen University, 2010.
17. F. Appel, R. Wagner, Mater. Sci. Eng. R 22 (1998) 187-268.
18. H. Inui, M. Oh, A. Nakamura, Acta Metal. Mater. 40 (1992) 3095-3104.
19. H. Inui, M. Matsumuro, D. H. Wu, M. Yamaguchi, Phil. Mag. A 75 (1997) 395-423.
20. M. Zupan, K. J. Hemker, Acta Mater. 51 (2003) 6277-6290.
21. M. A. Stucke, V. K. Vasudevan, D. M. Dimiduk, Mater. Sci. Eng. A 192/193 (1995) 111-119.
22. T. Kawabata, T. Kanai, O. Izumi, Acta Metall. 33 (1985) 1355-1366.
23. S. H. Whang, Q. Feng, Z. M. Wang, Intermetallics 8 (2000) 531-537.
24. M. Aindow, K. Chaudhuri, S. Das, H. L. Fraser, Scr. Metall. Mater. 24 (1990) 1105-1108.
25. B. K. Kad, H. L. Fraser, Phil. Mag. Lett. 70 (1994) 211-220.
26. D. B. Williams, C. B. Carter, Transmission Electron Microscopy, Plenum Press, 1996.
27. P. Chen, S. C. Mao, Y. Liu, F. Wang, Y. F. Zhang, Z. Zhang, X. D. Han, Mater. Sci. Eng. 580 (2013) 114-119.
28. Q. K. Zhang, Z. F. Zhang, Scr. Mater. 67 (2012) 289-292.

29. M. Ojima, Y. Adachi, S. Suzuki, Y. Tomota, Acta Mater. 59 (2011) 4177-4185.
30. G. G. E. Seward, S. Celotto, D. J. Prior, J. Wheeler, R. C. Pond. Acta Mater. 52 (2004) 821-832.
31. C. J. Boehlert, Z. Chen, I. Gutiérrez-Urrutia, J. Llorca, M. T. Pérez-Prado. Acta Mater. 60 (2012) 1889-1904.
32. S. I. Wright, M. Nowell. Eds. A. J. Schwartz, M. Kumar, B. L. Adams, D. P. Field. Electron Backscatter Diffraction in Materials Science, Springer, 2009.
33. L. Wang, Y. Yang, P. Eisenlohr, T. R. Bieler, M. A. Crimp, D. E. Mason. Metall. Mater. Trans. A 41 (2010) 421-430.
34. H. Li, D. E. Mason, Y. Yang, T. R. Bieler, M. A. Crimp, C. J. Boehlert, Phil. Mag. 93 (2013) 2875-.
35. C. J. Boehlert, H. Li, L. Wang, B. Bartha, Adv. Mater. Process. 168 (2010) 41-45.
36. J. Aguilar, A. Schievenbusch, O. Kättliz, Intermetallics 19 (2011) 757-761.
37. R. Gerling, H. Clemens, F. P. Schimasky, Adv. Eng. Mat. 6 (2004) 23-37.
38. Standard Test Methods for Determining Average Grain Size, ASTM Designation E112-96e3, ASTM, West Conshohocken, PA, 1996.
39. G. Cao, L. Fu, J. Lin, Y. Zhang, C. Chen, Intermetallics 8 (2000) 647-653.
40. S. R. Dey, A. Hazotte, E. Bouzy, Intermetallics 17 (2009) 1052-1064.
41. S. Zghal, S. Naka, A. Couret, Acta Mater. 45 (1997) 3005-3015.
42. J. B. Singh, G. Molénat, M. Sundararaman, S. Banerjee, G. Saada, P. Veyssière, A. Couret, Phil. Mag. 86 (2006) 2429-2450.
43. T. Fujiwara, A. Nakamura, M. Hosomi, S. R. Nishitani, Y. Shirai, M. Yamaguchi, Phil. Mag. A 61 (1990) 591-606.
44. H. Inui, M. H. Oh, A. Nakamura, M. Yamaguchi, Acta Metall. Mater. 40 (1992) 3095-3104.
45. M. Hazzledine, B. K. Kad, Mater Sci. Eng. A 192/193 (1995) 340-346.
46. C. Woodward, S. I. Rao, Phil. Mag. 84 (2004) 401-413.
47. T. G. Nieh, M. Wadsworth, O. D. Sherby, Superplasticity in metals and ceramics, Cambridge University Press, Cambridge, UK, 1997
48. M. F. Ashby, M. A. Verral, Acta Metal. 21 (1973) 149-163.
49. J. R. Spingarn, W. D. Nix, Acta Metal. 26 (1978) 1389-1398.
50. O. D. Sherby, J. Wadsworth, Prog. Mater. Sci. 33 (1989) 169-221.
51. A. Ball, M. M. Hutchison, Met. Sci. J. 3 (1969) 1-6.
52. K. Sotoudeh, P. S. Bate, Acta Mater. 58 (2010) 1909-1920.
53. M. A. Rust, R. I. Todd, Acta Mater. 59 (2011) 5159-5170.
54. H. Watanabe, K. Kurimoto, T. Uesugi, Y. Takigawa, K. Higashi, Phil. Mag. 93 (2013) 2913-2931.
55. M. T. Pérez-Prado, G. González-Doncel, O. A. Ruano, T. R. McNelley, Acta Mater. 59 (2001) 2905-2918.

	PMFC - Grains	PMFC - Lamellae
Group 1	15 %	8 %
Group 2	36 %	44 %
Group 3	49 %	48 %

Table 4. Fraction of traces corresponding to each group in PMFC grains and lamellae

Table 5. Reported CRSS values for γ-TiAl single crystal alloys.

Composition (at.%), [orientation of the tensile axis]	T(°C)	$CRSS_o$ (MPa)	$CRSS_s$ (MPa)	$R=CRSS_o/CRSS_s$	Reference
Ti-56Al, [$\mathbf{021}$]	700	160			[19]
Ti-56Al, [$\mathbf{001}$]	700		180	0.9	[19]
Ti-56Al, [$\mathbf{251}$]	700		100	1.6	[19]
Ti-56Al, [$\mathbf{\bar{1}52}$]	700		90	1.8	[19]
Ti-55.5Al, [$\mathbf{001}$]	600-		170		[20]
Ti-55.5Al, [$\mathbf{010}$]	600-		120		[20]
Ti-55.5Al, [$\mathbf{\bar{1}10}$]	600-		90		[20]
Ti-56Al, [$\mathbf{001}$]	600-		160		[21]
Ti-56Al, [$\mathbf{010}$]	600-		130		[21]
Ti-56Al, [$\mathbf{\bar{1}10}$]	600-		120		[21]
Ti-56Al, [$\mathbf{\bar{3}\ 12\ 7}$]	900	110			[23]
Ti-56Al, [$\mathbf{\bar{1}\ 6\ 3}$]	900	120			[23]
Ti-56Al, [$\mathbf{\bar{1}\ 12\ 5}$]	900	130			[23]
Ti-56Al, [$\mathbf{\bar{2}\ 4\ 7}$]	900		150		[23]
Ti-56Al, [$\mathbf{\bar{1}\ 6\ 12}$]	900		185		[23]
Ti-58Al, [$\mathbf{021}$]	25	175			[19]
Ti-58Al, [$\mathbf{\bar{1}52}$]	25		90	1.9	[19]
Ti-56Al, [$\mathbf{021}$]	25	165			[19]
Ti-56Al, [$\mathbf{\bar{1}52}$]	25		85	1.9	[19]
Ti-54Al, [$\mathbf{021}$]	25	140			[19]
Ti-54Al, [$\mathbf{\bar{1}52}$]	25		75	1.9	[19]
Ti-50Al, [$\mathbf{021}$]	25	45			[19]
Ti-50Al, [$\mathbf{\bar{1}52}$]	25		60	0.8	[19]

Slip Plane	Slip Direction	Dislocation Type
$\{\mathbf{111}\}$	$[1\bar{1}0]$	OD
$\{\mathbf{111}\}$	$[10\bar{1}]$	SD
$\{\mathbf{111}\}$	$[01\bar{1}]$	SD
$\{\bar{\mathbf{1}}\mathbf{11}\}$	$[\bar{1}\bar{1}0]$	OD
$\{\bar{\mathbf{1}}\mathbf{11}\}$	$[\bar{1}0\bar{1}]$	SD
$\{\bar{\mathbf{1}}\mathbf{11}\}$	$[0\bar{1}1]$	SD
$\{\mathbf{11}\bar{\mathbf{1}}\}$	$[1\bar{1}0]$	OD
$\{\mathbf{11}\bar{\mathbf{1}}\}$	$[101]$	SD
$\{\mathbf{11}\bar{\mathbf{1}}\}$	$[011]$	SD
$\{\mathbf{1}\bar{\mathbf{1}}\mathbf{1}\}$	$[110]$	OD
$\{\mathbf{1}\bar{\mathbf{1}}\mathbf{1}\}$	$[10\bar{1}]$	SD
$\{\mathbf{1}\bar{\mathbf{1}}\mathbf{1}\}$	$[011]$	SD

Table 1. Classification of γ- TiAl slip systems (OD: ordinary dislocation; SD: superdislocation) [16].

Sample	σ_{max} (MPa)	ε_{max} (%)
CC - 580 ºC	458	1.3
CC - 700 ºC	549	1.6
CCFC - 580 ºC	437	1.8
CCFC - 700 ºC	497	1.9

Table 2. Maximum flow stress and the elongations to failure of tensile tested CC and CCFC material at 580 ˚C and 700 ˚C.

	CCFC	PMFC
Group 1	17 %	13 %
Group 2	31 %	38 %
Group 3	52 %	49 %

Table 3. Fraction of traces corresponding to each group in CCFC and PMFC materials.

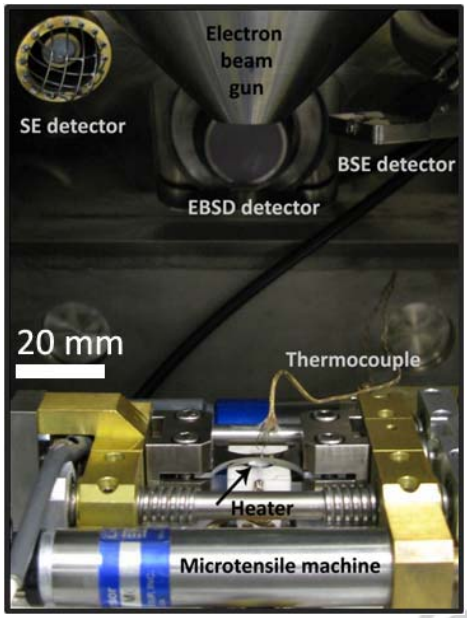

(a)

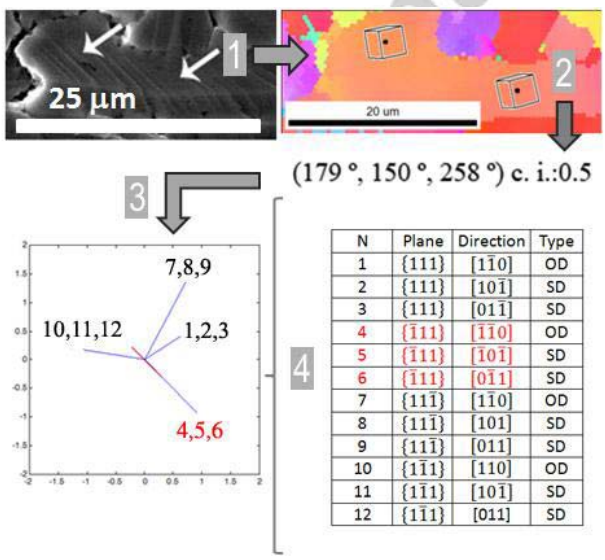

N	Plane	Direction	Type
1	{111}	[1$\bar{1}$0]	OD
2	{111}	[10$\bar{1}$]	SD
3	{111}	[01$\bar{1}$]	SD
4	{$\bar{1}$11}	[$\bar{1}$10]	OD
5	{$\bar{1}$11}	[$\bar{1}$0$\bar{1}$]	SD
6	{$\bar{1}$11}	[0$\bar{1}$1]	SD
7	{11$\bar{1}$}	[1$\bar{1}$0]	OD
8	{11$\bar{1}$}	[101]	SD
9	{11$\bar{1}$}	[011]	SD
10	{1$\bar{1}$1}	[110]	OD
11	{1$\bar{1}$1}	[10$\bar{1}$]	SD
12	{1$\bar{1}$1}	[011]	SD

(b)

Fig 1. (a) Microtensile testing machine inside the SEM chamber; (b) Slip mode analysis: 1-Slip trace identification by *in situ* SEM; 2-Measurement of the Euler angles in the studied region by EBSD; 3-Calculation of the traces corresponding to the 12 available slip systems;,4-Selection of the possible slip systems associated to an experimentally observed slip trace. Note that in this example slip systems 4,5,6 were all parallel to the slip trace.

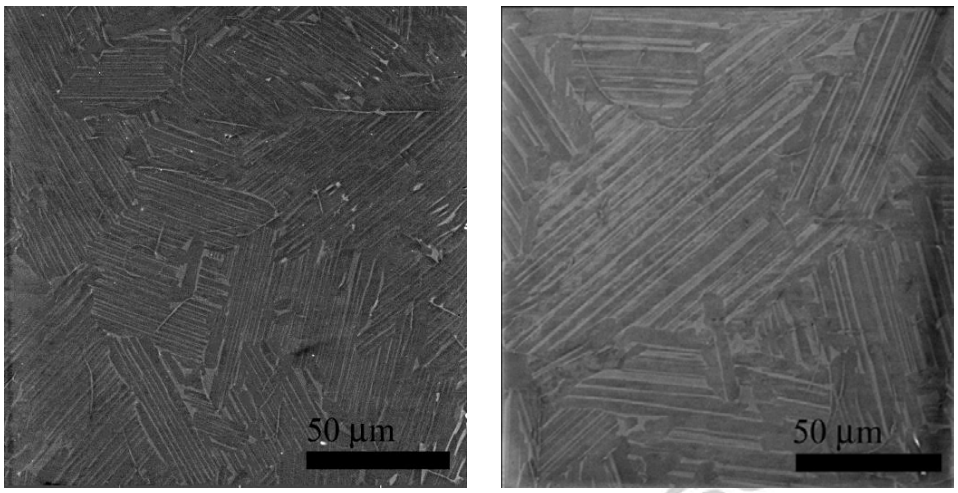

(a) (b)

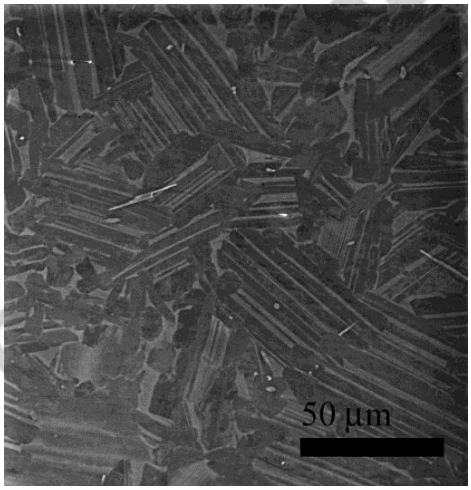

(c)

Fig 2. BSE SEM images of the Ti4522XD alloy (a) processed by centrifugal casting (CC); (b) centrifugally cast, heat treated at 1300 °C for 2 h and furnace cooled (CCFC); (c) processed by powder metallurgy by HIP from prealloyed powders, subsequently heat treated at 1300 °C for 2 h and then furnace cooled (PMFC).

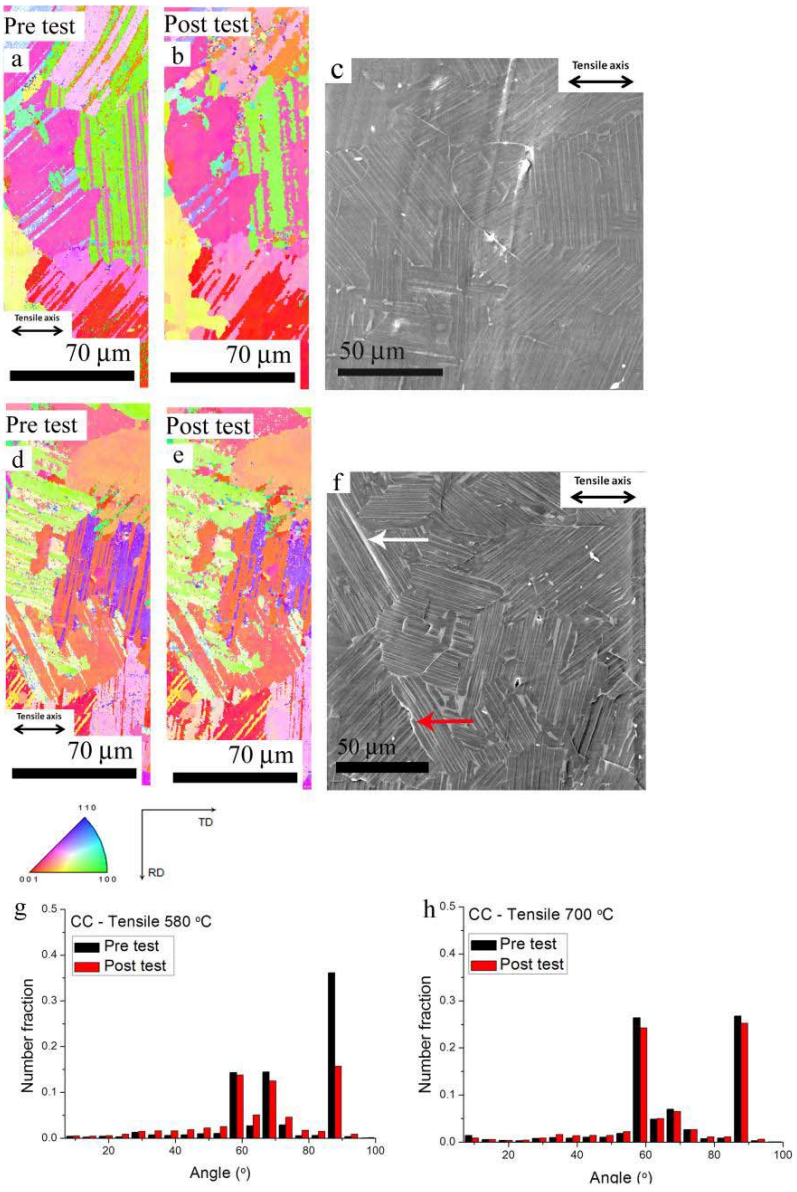

Fig 3. EBSD inverse pole figure maps in the ND and BSE SEM micrographs corresponding to selected areas of the CC microstructure: (a) before and (b, c) after the tensile test at 580 °C, σ_{max}= 458 MPa, ε_{max}= 1.3 %; (d) before and (e, f) after the tensile test at 700 °C, σ_{max}= 549 MPa, ε_{max}= 1.6 %. (g,h) Comparison of the misorientation distribution histograms in those same areas before and after the tensile tests at 580 °C (g) and at 700 °C (h).

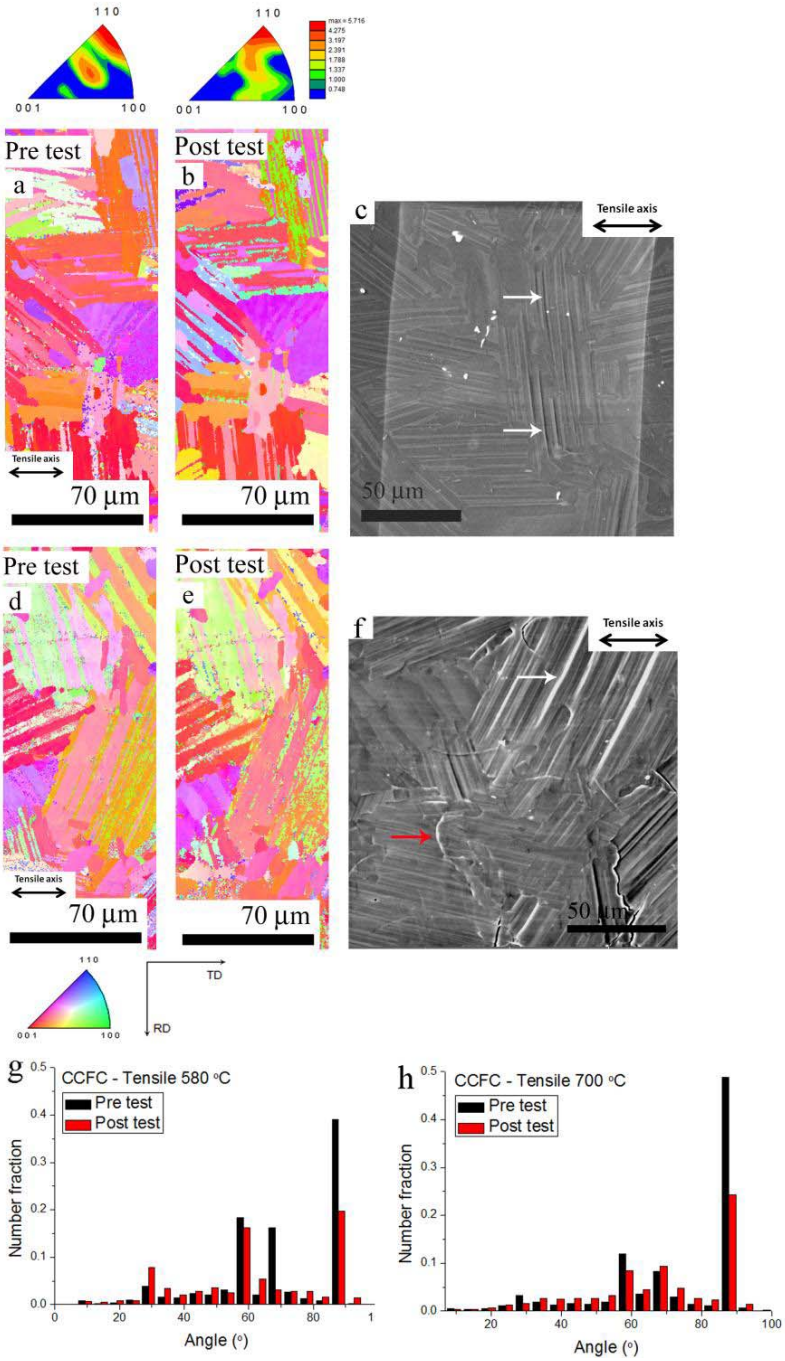

Fig 4. EBSD inverse pole figure maps in the ND and BSE SEM micrographs corresponding to selected areas of the CCFC microstructure: (a) before and (b, c) after the tensile test at 580 °C, σ_{max}= 437 MPa, ε_{max}= 1.8 %, including the corresponding inverse pole figures showing the orientation of the tensile axis; (d) before and (e, f) after the tensile test at 700 °C, σ_{max}= 497 MPa, ε_{max}= 1.9 %. (g, h) Comparison of the misorientation distribution histograms in those same areas before and after the tensile tests at 580 °C (g) and at 700 °C (h).

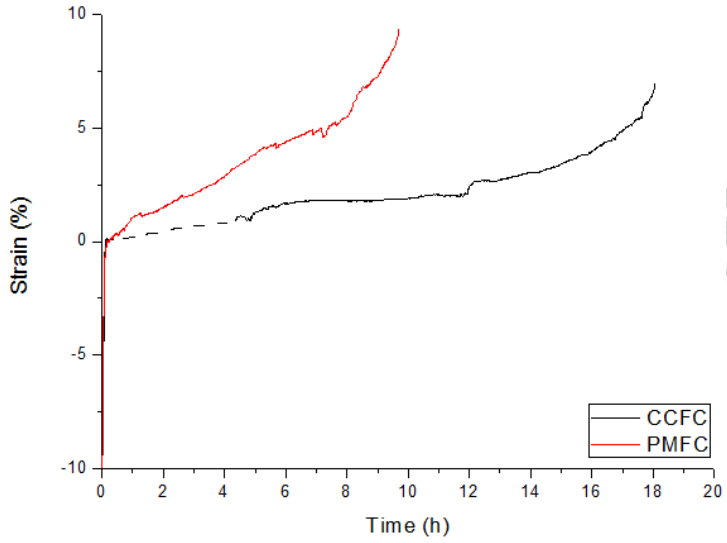

(a)

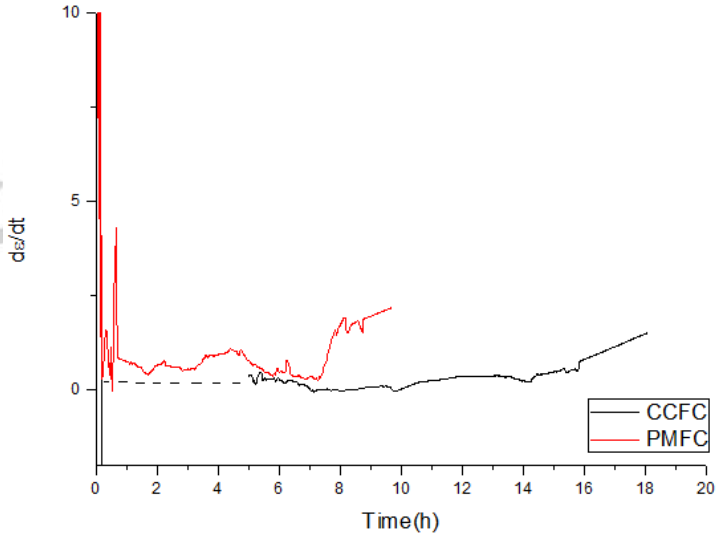

Fig 5. (a) Strain versus time and (b) strain rate versus time curves corresponding to the CCFC and the PMFC microstructures deformed in tension at 700 °C and at a constant stress of 65%σ_{UTS};

Figure 6

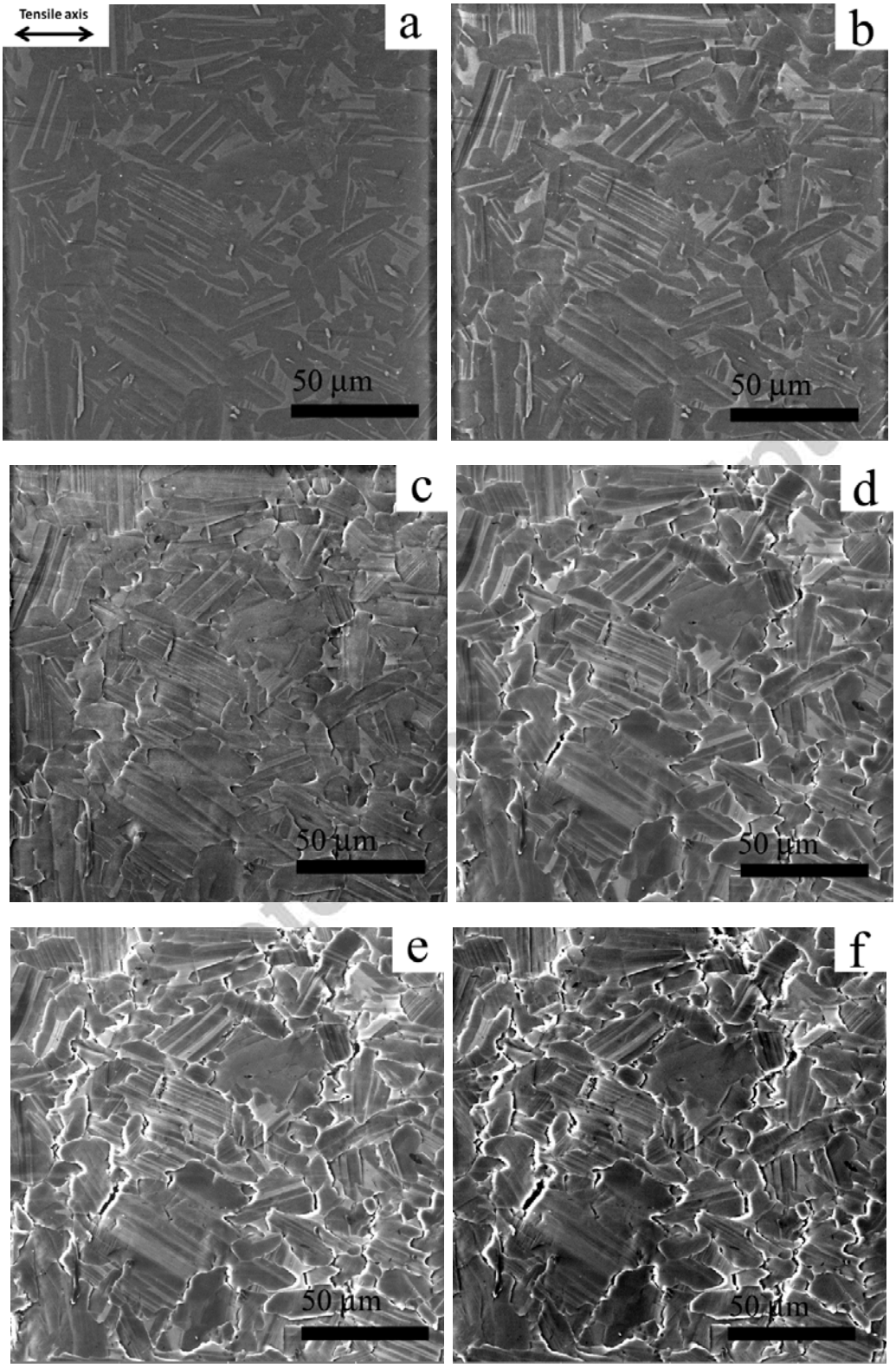

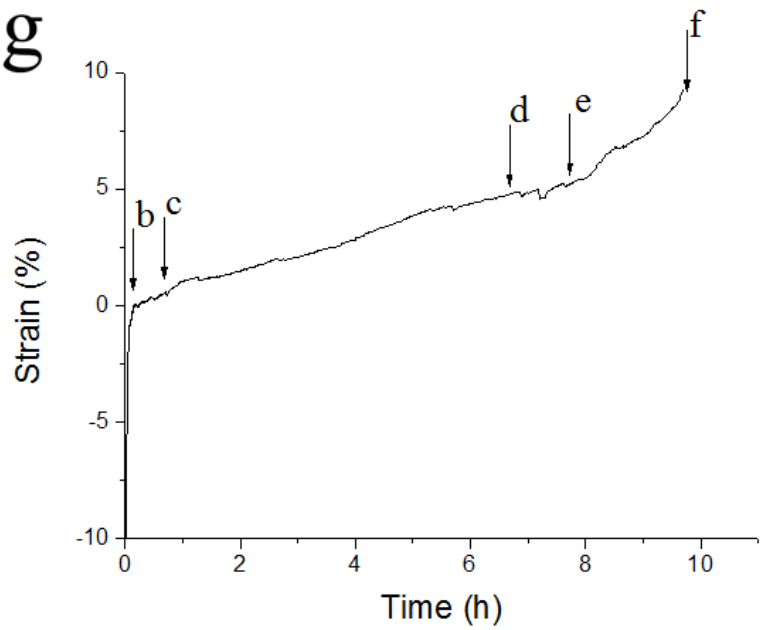

Figure 6 Sequence of SEM micrographs showing the evolution of the PMFC microstructure during creep straining at 700°C. (a) 0 h; (b) 0.3 h, ε≈0.1 %; (c) 1.0 h, ε≈1.0 %; (d) 7.0 h, ε≈5.0 %; (e) 8.3 h, ε≈6.2 %; (f) 9.7 h, ε_{max}≈9.4 %; (g) Corresponding total strain versus time curve indicating the strains at which the (b)-(f) SEM images were taken.

Figure 7

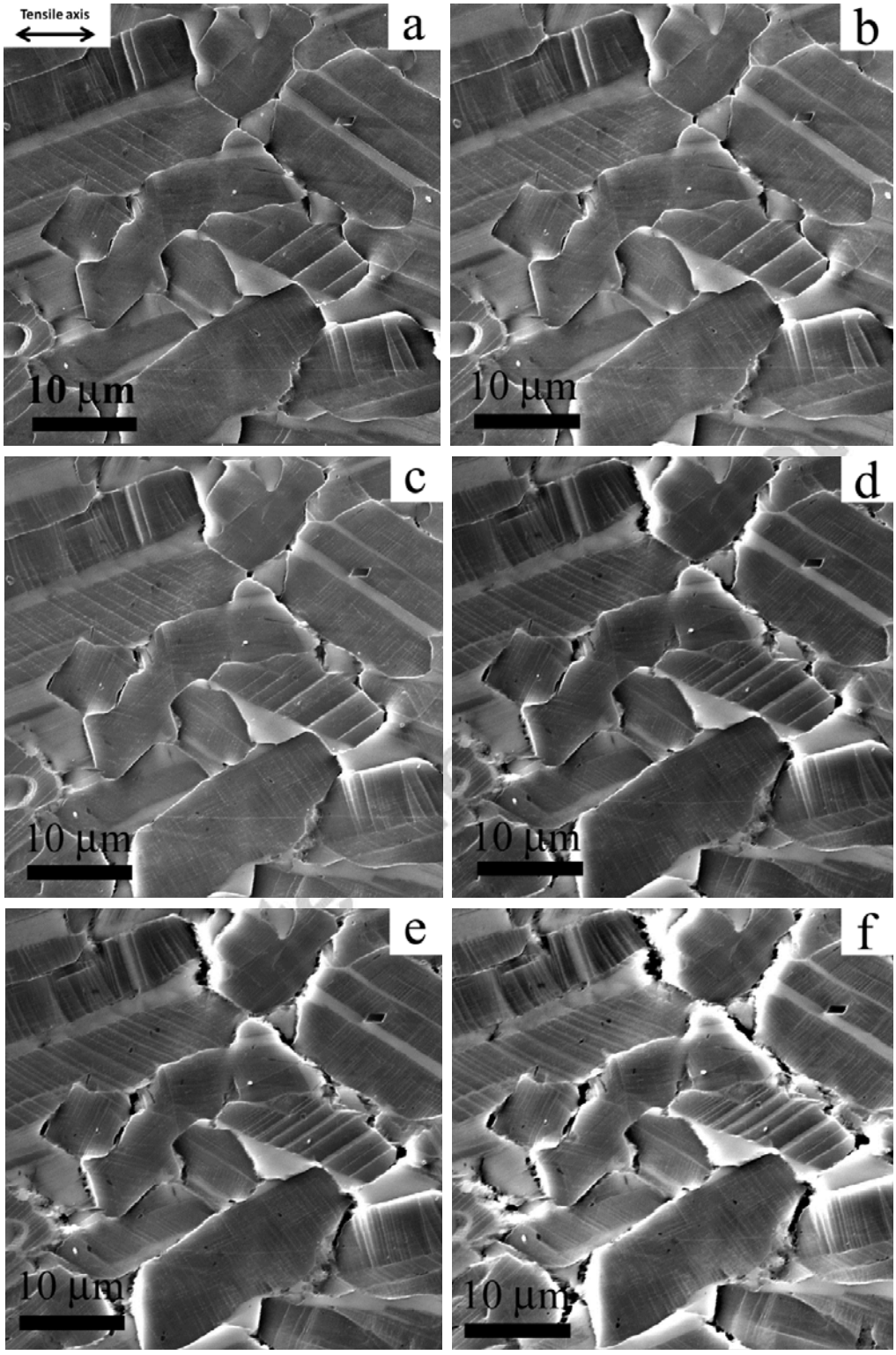

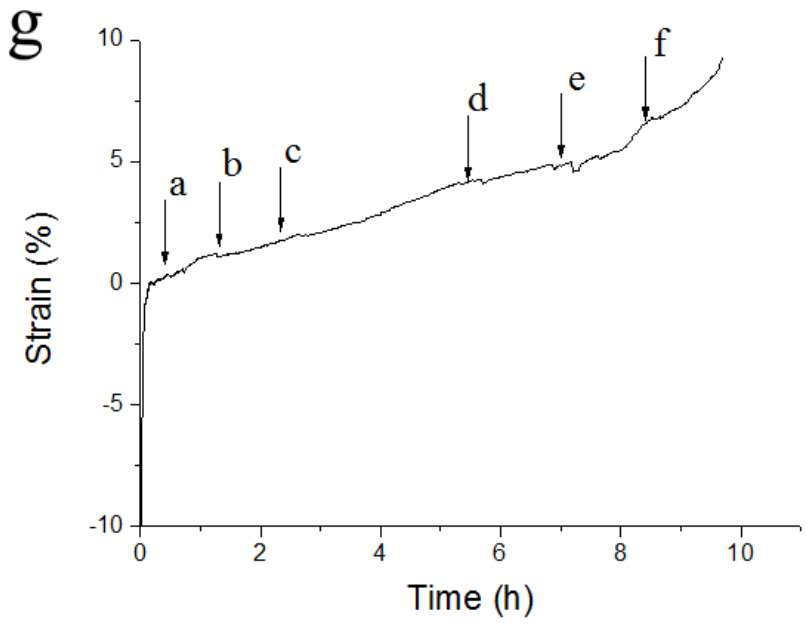

Figure 7. Sequence of SEM micrographs showing the evolution of the surface of the PMFC sample during creep straining at 700°C. (a) 0.8 h, ε≈0.7 %; (b) 1.3 h, ε≈1.1 %; (c) 2.7 h, ε≈2.0 %; (d) 5.8 h, ε≈4.2 %; (e) 7.3 h, ε≈4.6 %; (f) 8.6 h, ε≈6.8 %; (g) Corresponding total strain versus time curve indicating the strains at which the (a)-(f) SEM images were taken.

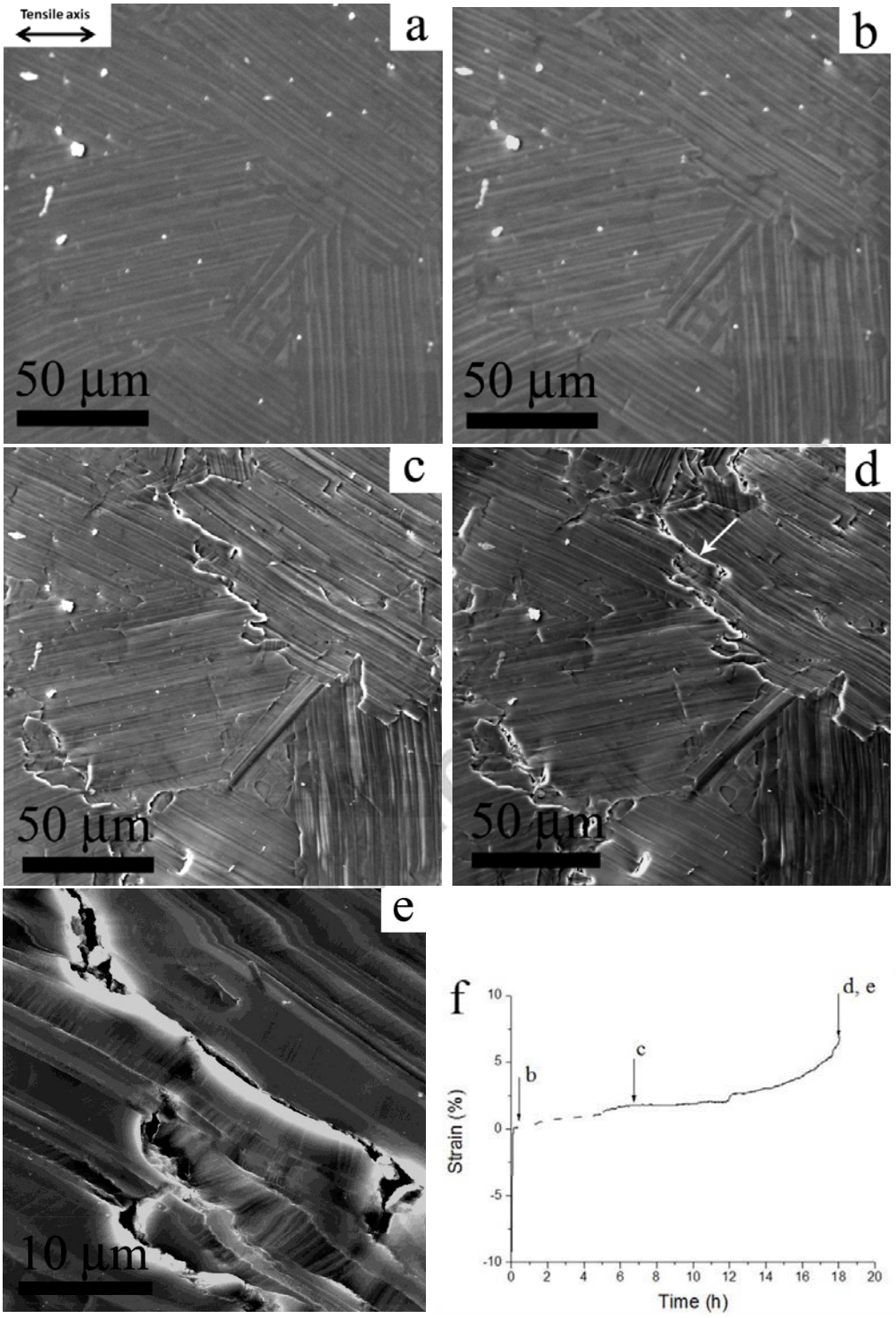

Figure 8. Sequence of SEM micrographs showing the evolution of the surface of the CCFC sample during creep straining at 700°C. (a) 0 h; (b) 0.5 h, ε≈0.3 %; (c) 7.0 h, ε≈1.8 %; (d, e) 18.1 h, ε_{max}≈7.0 %; (e) higher magnification SE SEM micrograph from the area pointed with the arrow in (d); (f) Corresponding total strain versus time curve indicating the strains at which the(b)-(e) SEM images were taken.

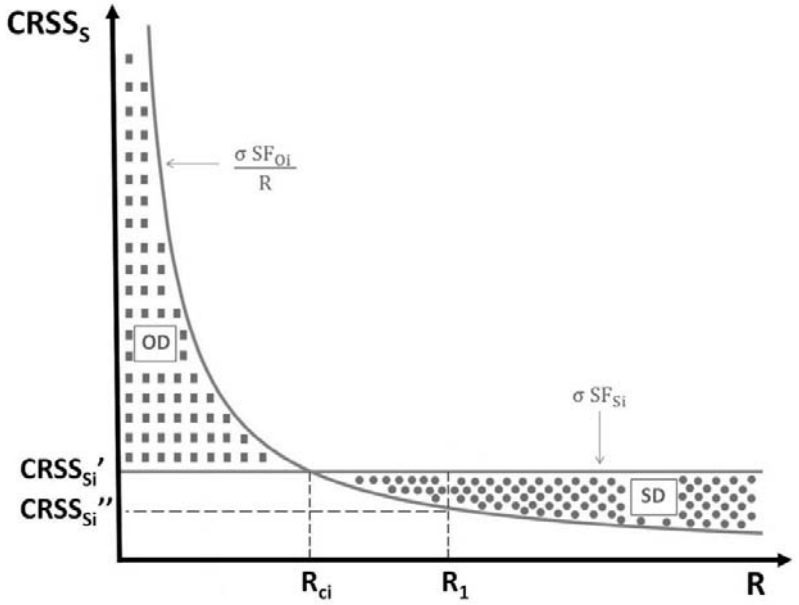

Fig 9. Schematic showing the variation of $CRSS_s$ with respect to R for a given trace t_i. The shaded areas correspond to ($CRSS_s$,R) pairs for which ordinary (OD) and superdislocations (SD) are active. R_{ci} is a critical R value which marks the transition from ordinary to superdislocation slip.

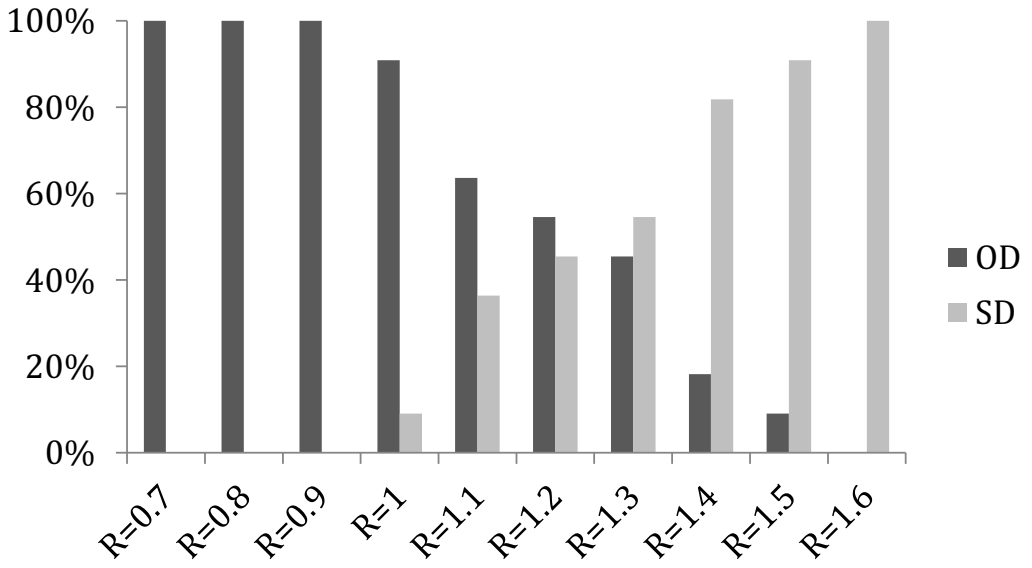

Fig 10. Relative activity of OD and SD for different R values in the gamma grains of the duplex microstructure (PMFC) during creep at 700°C and 300 MPa.